

# Optics Letters

## Deep line-temporal focusing with high axial resolution and a large field-of-view using intracavity control and incoherent pulse shaping

KAI LOU,<sup>1</sup>  BO WANG,<sup>2</sup> AH-YOUNG JEE,<sup>1</sup> STEVE GRANICK,<sup>1,3,4</sup>  AND FRANÇOIS AMBLARD<sup>1,3,5</sup> 

<sup>1</sup>IBS Center for Soft and Living Matter, Ulsan, South Korea

<sup>2</sup>Department of Bioengineering, Stanford University, Stanford, California 94305, USA

<sup>3</sup>UNIST (Ulsan National Institute of Science and Technology), Ulsan, South Korea

<sup>4</sup>e-mail: sgranick@ibs.re.kr

<sup>5</sup>e-mail: famblard@protonmail.com

Received 8 August 2018; revised 31 August 2018; accepted 1 September 2018; posted 10 September 2018 (Doc. ID 341776); published 5 October 2018

Line-temporal focusing has been recognized as an elegant strategy that provides two-photon microscopy with an effective means for fast imaging through parallelization, together with an improved resilience to scattering for deep imaging. However, the axial resolution remains sub-optimal, except when using high NA objectives and a small field-of-view. With the introduction of an intracavity control of the spectral width of the femtosecond laser to adaptively fill the back aperture of the objective lens, line-temporal focusing two-photon microscopy is demonstrated to reach near-diffraction-limited axial resolution with a large back-aperture objective lens, and improved immunity to sample scattering. In addition, a new incoherent flattop beam shaping method is proposed which provides a uniform contrast with little degradation of the axial resolution along the focus line, even deep in the sample. This is demonstrated in large volumetric imaging of mouse lung samples. © 2018 Optical Society of America

**OCIS codes:** (320.5540) Pulse shaping; (170.3660) Light propagation in tissues; (180.6900) Three-dimensional microscopy; (290.7050) Turbid media.

<https://doi.org/10.1364/OL.43.004919>

The many interesting capabilities and applications of two-photon fluorescence microscopy [1,2] are known to involve tradeoffs between the selective achievement of outstanding imaging resolution [3,4], speed [5,6], and penetration depth [7–9]. The seminal demonstration with one or multiple discrete focal points in one focal plane established the proof of concept [10,11], while later developments ensued, motivated by improving resolution, imaging depth, speed, field-of-view (FOV), or immunity to tissue scattering. A major conceptual step was introduced in the field of nonlinear optical microscopies in general with the notion of temporal focusing, i.e., by

using the contrast produced by reducing the duration of the femtosecond laser pulses while focusing [6,7,12–15].

In nonlinear optical microscopies with femtosecond lasers, the time-averaged response depends not only on the average intensity of the laser, but also on its temporal compression ratio, i.e., on how much the optical energy is temporally compressed into ultrashort pulses. Put in simple terms, the time-averaged local density of nonlinear effects of order  $n$  ( $\geq 2$ ) created at position  $\mathbf{r}$  scales as  $I^n(\mathbf{r})g^{n-1}(\mathbf{r})$ , where  $I(\mathbf{r})$  is the time-averaged excitation intensity, and  $g(\mathbf{r}) = \tau_F/\tau(\mathbf{r})$  is the temporal compression ratio derived from the interpulse repetition time-interval  $\tau_F$  and the pulse duration  $\tau(\mathbf{r})$  which possibly depends on space [16,17]. In the classical two-photon laser-scanning microscopy (TP-LSM), a circular femtosecond laser beam fills the objective back aperture to generate a focal spot, and the pulse duration is set by its value  $\tau_R$  at the laser output. Because  $\tau(\mathbf{r})$  is practically uniform throughout the sample with  $\tau(\mathbf{r}) = \tau_R$ , the temporal compression ratio is uniform, and the contrast function is proportional to  $I^2(\mathbf{r})$ .

However, in nonlinear microscopies with temporal focusing, the temporal compression ratio  $g(\mathbf{r})$  is designed to be nonuniform along the light path so as to create an independent source of contrast. An optical diffraction element such as a blazed grating [12] or a digital micromirror [18] is used to spatially disperse the spectral components of the femtosecond beam prior to entering the microscope objective. Subsequently, these spatially dispersed spectral components are refocused to gradually overlap and interfere in the focal plane and restore the initial femtosecond pulse duration [19]. Temporal focusing two-photon microscopy was first introduced as a scanless technique that provides the simultaneous excitation of an extended 2D focus, in which the axial sectioning is solely produced by pulse shaping along the  $z$ -axis [12]. Thanks to a poor temporal compression ratio at the entry surface of the objective, the out-of-focus fluorescence is much reduced, leading to an improved penetration depth when compared to TP-LSM [20]. However, 2D temporal focusing is restricted to small focus applications because it requires a laser power that is orders of magnitude

higher than point scanning [17], thus creating potential photo-damage of the specimen.

A second mode of temporal focusing has been proposed by combining it with line focusing [9,21,22]. Instead of producing an extended 2D focus from a continuous series of light spots (spectral components) in the back aperture of the objective, a line is produced in the focal plane by creating a series of line beams (spectral components) in the back aperture of the objective. The consequence of combining 1D spatial focusing with temporal focusing in the perpendicular direction is to combine  $I(\mathbf{r})$  and  $g(\mathbf{r})$  in a more balanced way. The so-called line-temporal focusing microscopy (LTFM) obtained by 1D scanning the line focus leads to a unique combination of advantages: an improved speed and penetration depth when compared to TP-LSM, a better resilience to scattering and axial resolution when compared to 2D-temporal focusing, as well as lower laser power [9]. Thus, while LTFM represents an attractive compromise with respect to imaging speed and depth, scattering resilience, and axial resolution, the FOV remains limited. In addition, it is hard, especially for objectives with a large back aperture, to reach the near diffraction-limited axial resolution that is a significant virtue of two-photon fluorescence microscopy.

The novelty of this Letter is the co-optimization of the axial resolution and the uniformity of the contrast over a large FOV for large-aperture objectives. The optical system is shown in Fig. 1(a), and it relies on two major ingredients: 1) optimization of the size of the rainbow beam composed of the spatially dispersed spectral components for the aperture fill factor by adaptive control of the femtosecond laser spectrum, to improve the axial resolution and its resilience to scattering; 2) production of a long and uniform focal line by a dedicated femtosecond beam shaping method to broaden the FOV. The key element for LTFM is to shape the femtosecond laser beam so as to focus it on the objective back aperture (radius  $R$ ) as a series of line beamlets (spectral components), with a length  $2b$  in the spatial focusing direction and a much smaller width  $2a$  ( $b \gg a$ ) in the temporal focusing direction, as shown in Fig. 1(b). In the experiment, a spherical collimating lens with a focal length of  $f_L$  is used to generate a line beam  $a = \lambda f_L / \pi b$ . While the contribution of spatial focusing to the axial resolution depends on the effective spatial fill factor  $b/R$ , the contribution of temporal focusing depends on the effective temporal radius  $a_T = \sqrt{a^2 + (\beta\Omega)^2}$  [14], where  $\beta$  is a constant depending on the focal length of the collimating lens and the grating period, and  $\Omega$  is the full-width at half-maximum (FWHM) of the femtosecond laser spectrum.

The resulting optimization dilemma for a given diffraction grating and spectral width  $\Omega$ , is that an increase of the focal length  $f_L$  increases both  $a_T$  and  $a$  simultaneously, thus leading respectively to a better axial resolution but a shorter focal line and smaller FOV. In other words, better axial resolution comes at the expense of a smaller FOV.

To resolve this dilemma and independently maximize the FOV ( $a \rightarrow \lambda$ ) and the axial resolution ( $b$  and  $a_T \rightarrow R$ ), we propose a setup in which the width  $\Omega$  of the laser spectrum can be independently adjusted, with no impact on the purely geometric parameters  $a$  and  $b$ . This is achieved by an intracavity control of the width of the femtosecond laser spectrum [Fig. 1(a)]. The femtosecond laser with a central wavelength of 800 nm, a repetition rate of 80 MHz, an initial spectrum of  $\Omega = 6.9$  nm

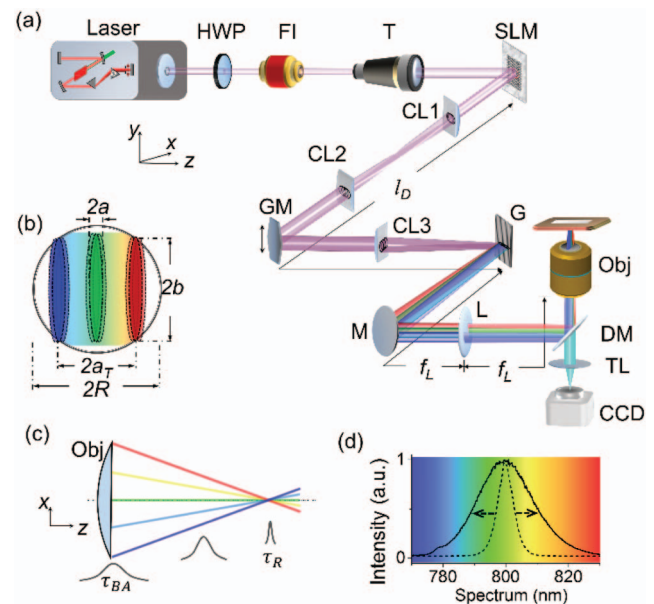


**Fig. 1.** Schematic diagram of the system implemented. (a) Output from a femtosecond laser. The laser power was controlled using a half-wave plate (HWP) and a Faraday isolator (FI). The beam was expanded by a telescope (T), impinged on a SLM, passed through an afocal cylindrical lens pair (CL1 and CL2), and then reflected from a 1D GM and focused through another cylindrical lens (CL3, focal length  $f_L$ ) onto a 1200 line/mm blazed grating (G). The spectral components dispersed by the grating were collected by a spherical collimating lens (L, focal length  $f_L$ ) and reflected by a dichroic mirror (DM) into a water-immersion objective lens (10x, NA0.45). The fluorescence emission passed through the objective, a tube lens (TL), and an emission filter before being detected by an electron-multiplication CCD camera (EMCCD). (b) Schematic representation of the spatially dispersed spectral components at the objective back aperture (radius  $R$ ). Each diffraction order is similarly dispersed by G, but with a slightly different incidence angle. The spatial and temporal fill factors are  $b/R$  and  $a_T/R$  respectively, in the  $x$  and  $y$  directions. (c) Schematic diagram of the dispersed spectral components passing through the objective, where  $\tau_{BA}$  and  $\tau_R$  are the pulse durations at the back aperture and focal plane of the objective. (d) Effect of the intracavity control on the spectral width of the laser. The initially narrow spectrum ( $\Omega = 6.9$  nm, dotted curve) broadens up to a maximum one ( $\Omega = 21.4$  nm, solid curve) used for comparison experiments.

(pulse duration 160 fs), and a pulse energy 36 nJ was used for photoexcitation. In the cavity of the femtosecond laser, a computer-program controlled the prism pair compressor and the slit so that the spectrum could be modulated by adjusting the prism pair angle and the slit width [23]. The laser spectrum was measured using a fiber spectrometer. A prism compressor is placed at the laser exit to precompensate for group velocity dispersion (GVD) throughout the optical system. The beam is expanded in the  $y$ -direction with an afocal pair of cylindrical lenses (CL1 and CL2), and shaped in the  $x$  direction with a spatial light modulator (SLM) to produce a flattop beam. The beam-shaped light is then focused by a cylindrical lens (CL3, focal length  $f_L$ ) as a flattop line on the grating, after a 1D galvanometer mirror (GM) used to scan that line perpendicularly to itself. That line is Fourier transformed by a spherical collimating lens (L) to produce a spatially chirped pattern of

line beams [Fig. 1(b)] which, in turn, are focused to produce the line focus. Fluorescence emission is detected by an EMCCD. For a given grating and collimating lens, the coefficient and  $\beta$  and the pulse duration  $\tau_{BA}$  in the objective back aperture do not depend on  $\Omega$ . Meanwhile, since the time-bandwidth product  $\tau_R \Omega$  is constant for nonchirped pulses, one expects in the focal plane that the pulse duration  $\tau_R$  and the temporal compression ratio  $g(r)$  both scale as  $\Omega^{-1}$  [Fig. 1(c)]. As a consequence, if the GVD is properly compensated for at the focus, the contrast produced between the back aperture and the focal plane by the function  $I^2(r)g(r)$  for increasing values of  $\Omega$  [Fig. 1(d)], should significantly increase because of an enhanced temporal compression and a larger beam size  $a_T$ .

Practically, our LTFM setup was first implemented with a 6.9 nm FWHM laser spectrum (pulse duration of 160 fs), a 1200 line/mm blazed grating, and cylindrical lens CL3 and collimating lens L with the same focal length of 500 mm. A series of line beamlets was produced on the back aperture, with a strong focus in the  $xz$ -plane and collimated in the  $yz$  plane, with typical radii  $(a, b) = (21 \mu\text{m}, 6 \text{ mm})$ . A length of 300  $\mu\text{m}$  was obtained after the objective and the resulting FOV 300  $\mu\text{m} \times 800 \mu\text{m}$  after 1D scanning. In these conditions, which correspond to underfilling the aperture in the temporal focusing scheme, axial optical sectioning at FWHM was measured as 7.9  $\mu\text{m}$  with dilute fluorescent latex beads, 0.5  $\mu\text{m}$  in diameter, with a 1:1000 volume fraction in agarose [Fig. 2(a)]. Such a resolution is better than 1D line scanning in our laboratory (diamond), but worse than TP-LSM (star).

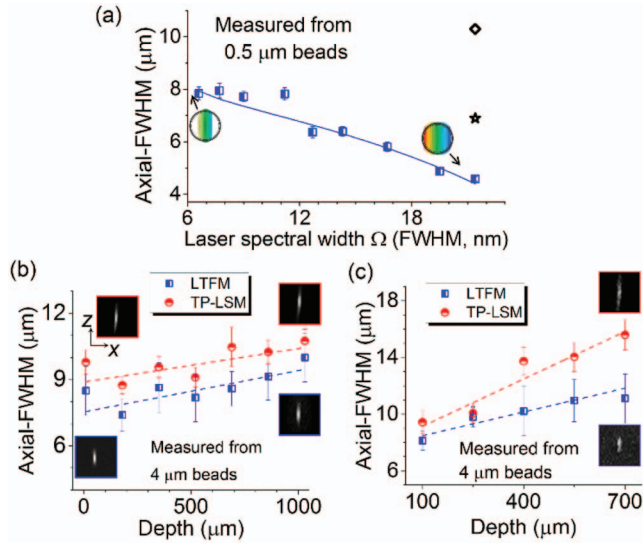


**Fig. 2.** Axial sectioning for two-photon point scanning and LTFM implemented here with the same laser, objective, and samples. (a) Axial FWHM, plotted against the laser spectral width  $\Omega$  with  $f_L = 500 \text{ mm}$ , using a  $10\times$  objective lens with  $\text{NA} = 0.45$ . The sample is made of 0.5  $\mu\text{m}$  diameter fluorescent beads immobilized at 0.1 mg/mL in agarose. Blue, line temporal focusing. Star, point scanning. Diamond, classical line scanning. (b), (c) Axial FWHM is shown as a function of imaging depth using LTFM (blue) and TP-LSM (red) modalities implemented in our laboratory with the same laser, objective ( $10\times$ ,  $\text{NA} = 0.45$ ), and same samples (4  $\mu\text{m}$  fluorescent beads dispersed in diluted intralipid emulsions). (b) and (c) correspond to a 1:1000 and 1:100 intralipid dilution respectively. Insets show  $x$ - $z$  sections of the point spread functions for different depths.

Nonetheless, when broadening the laser spectrum, the axial resolution was very significantly reduced, down to 4.5  $\mu\text{m}$  for  $\Omega = 21.4 \text{ nm}$  (pulse duration of 85 fs) without any reduction of the FOV.

The resilience of line-temporal focusing to sample scattering has been reported to be better than temporal focusing, but not as good as that for classical point focusing like TP-LSM [9]. Using a moderately scattering intralipid solution, we found similar results for TP-LSM and LTFM up to 1 mm deep, with practical slight degradation of the axial resolution with imaging depth [Fig. 2(b)]. However, in a strongly scattering intralipid solution, the same comparison shows that the axial resolution of LTFM is significantly more robust to scattering than TP-LSM up to 700  $\mu\text{m}$  deep in the sample [Fig. 2(c)].

The second improvement proposed here is aimed at overcoming the nonuniform photoexcitation produced by the Gaussian intensity profile along the line focus. There is no simple solution, since truncation of the Gaussian profile is known to degrade the axial resolution [7], and the customary Fourier shaping would introduce a phase modulation that is not compatible with temporal focusing. To overcome this problem and produce a “flat” intensity, we used a phase-only SLM to create three discrete diffracted beams. While the SLM selectively modulated the light in the  $xz$ -plane, an afocal pair of cylindrical lens, CL1 and CL2, selectively expanded the beam in the

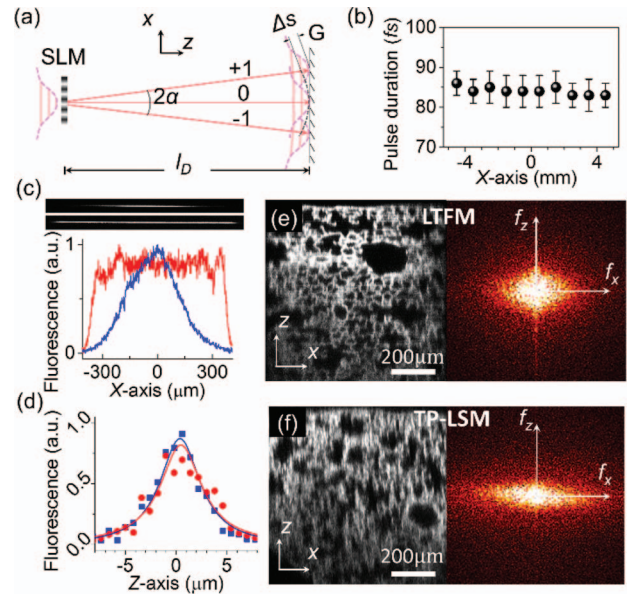


**Fig. 3.** Uniform photoexcitation. (a)  $xz$ -section diagram of the beam path between SLM and G. The three diffracted beam orders (0,  $\pm 1$ ) generated by an SLM focus through CL3 as three slightly offset adjacent line beams on G, that are conjugated to three adjacent lines in the sample focal plane. (b) Duration of laser pulses on the grating plotted against  $x$ -positions with active flattop beam generation. (c) Fluorescence response profiles along  $x$  for line temporal focusing without (top image and blue line) or with flattop photoexcitation (bottom image and red line) using a  $10\times$ ,  $\text{NA} = 0.45$  objective. (d) Axial fluorescence profiles of Gaussian (blue squares) and flattop (red circles) measured from 0.5  $\mu\text{m}$  diameter fluorescence beads. The  $xz$ -section of a  $780 \times 780 \times 900 \mu\text{m}^3$  volumetric image taken from a mouse lung slice respectively by (e) LTFM and (f) TP-LSM using the same  $10\times$  objective with  $\text{NA} = 0.45$ . The corresponding Fourier transform images are compared on the right of each image.



$yz$ -plane to control the fill factor of the back aperture [Figs. 1(a) and 3(a)]. A phase function written as  $t(\xi) = (1 + \gamma \cos(2\pi\xi/d + \varphi_0))/2$  was applied, where  $d$  is the spatial period,  $\gamma$  is the modulation depth, and  $\varphi_0$  is the initial phase [24]. The input beam therefore splits into three diffraction orders ( $0, \pm 1$ ). Given the distance  $l_D$  between the SLM and G, the spatial period was chosen to create a diffraction angle ( $2\alpha \approx 0.24^\circ$ ) so that the intensity distributions added to approximate a flattop. Importantly, the resulting angular dispersion comes with negligible chromatic dispersion ( $2.5 \times 10^{-3}\alpha$ ), thus avoiding variations of the pulse duration along the  $x$ -axis, as shown in Fig. 3(b). The individual intensities add on the grating provided adjacent diffraction orders create mutually incoherent optical fields in the same  $xy$  plane. This happens when the temporal coherence length of the laser  $s_T = \lambda^2/2\pi\Omega$  [25] is less than the optical path difference  $\Delta s = \lambda^2 l_D/2d^2$  between adjacent diffraction orders. Each of the three beams independently carries negligible chromatic dispersion, and each independently undergoes the same temporal focusing scheme. Consequently, their incoherently superimposed intensities generate a flattop beam at the focal plane. By using a broad enough spectrum ( $>11.4$  nm), the condition incoherence  $\Delta s > s_T$  was met, and a flattop beam width of  $780 \mu\text{m}$  was obtained, wider than the Gaussian mode of  $300 \mu\text{m}$  [Fig. 3(c)]. It is obvious that flattop shaping did not degrade the axial FWHM. With the  $10\times$  NA 0.45 objective and  $0.5 \mu\text{m}$  diameter fluorescent beads, the axial resolution was found to be  $4.5 \mu\text{m}$  for both Gaussian and flattop beams, which is very close to the diffraction limit, as shown in Fig. 3(d). Finally, a 1D GM was used to scan the line beam to acquire a wide FOV. As implemented here, by writing the appropriate phase ( $d = 7.1$ ,  $\gamma = 1.05$ ) on the spatial light modulator, photoexcitation extends uniformly over the FOV  $780 \times 800 \mu\text{m}^2$  when using a  $10\times$ , NA = 0.45 water immersion objective lens. These findings of successful deep imaging, despite scattering, are consistent with previous reports [3,7], showing that temporal focusing in biological tissues significantly reduces degradation of the point spread function by refraction index heterogeneities.

Finally, the imaging performance of this system was tested by volumetric imaging ( $780 \times 780 \times 900 \mu\text{m}^3$ ) of mouse lung slices labeled with fluorescent lectins [Fig. 3(e)] with the femto-second laser measured as  $1.4$  nJ/pulse at the back aperture of the objective. When comparing  $xz$ -sections from similar regions below the surface, 3D architecture was significantly better resolved using the present method than using two-photon laser scanning microscopy in our laboratory (with  $0.6$  nJ/pulse), as shown in Fig. 3(f). Fourier transforms of the  $xz$ -sections are shown on the right side of each image. Obviously, the

intracavity control of the femtosecond laser spectrum has enabled more isotropic volumetric resolution. Further tests of the method indicated that these conclusions hold for other objectives large-aperture with close to diffraction-limited axial resolutions, namely  $2.9 \mu\text{m}$  for a high NA dry objective ( $20\times$ , NA 0.8), and  $0.8 \mu\text{m}$  for an oil immersion objective ( $40\times$ , NA 1.3).

**Funding.** Institute for Basic Science (IBS) (IBS-R020-D1).

**Acknowledgment.** B. Wang holds a Career Award from the Burroughs Wellcome Fund. K. Lou thanks the Shenzhen Shineway Hi-Tech Co., Ltd for discussions on the technique.

## REFERENCES

1. F. Helmchen and W. Denk, *Nat. Methods* **2**, 932 (2005).
2. K. Svoboda and R. Yasuda, *Neuron* **50**, 823 (2006).
3. N. Ji, D. E. Milkie, and E. Betzig, *Nat. Methods* **7**, 141 (2010).
4. E. J. Botcherby, C. W. Smith, M. M. Kohl, D. Debarre, M. J. Booth, R. Juskaitis, O. Paulsen, and T. Wilson, *Proc. Natl. Acad. Sci. USA* **109**, 2919 (2012).
5. G. Katona, G. Szalay, P. Maák, A. Kaszás, M. Veress, D. Hillier, B. Chiovini, E. Vizi, B. Roska, and B. Rózsa, *Nat. Methods* **9**, 201 (2012).
6. T. Schrodell, R. Prevedel, K. Aumayr, M. Zimmer, and A. Vaziri, *Nat. Methods* **10**, 1013 (2013).
7. E. Papagiakoumou, V. de Sars, D. Oron, and V. Emiliani, *Opt. Express* **16**, 22039 (2008).
8. J. H. Park, W. Sun, and M. Cui, *Proc. Natl. Acad. Sci. USA* **112**, 9236 (2015).
9. H. Dana, N. Kruger, A. Ellman, and S. Shoham, *Opt. Express* **21**, 5677 (2013).
10. W. Denk, J. H. Strickler, and W. W. Webb, *Science* **248**, 73 (1990).
11. J. Bewersdorff, R. Pick, and S. W. Hell, *Opt. Lett.* **23**, 655 (1998).
12. D. Oron, E. Tal, and Y. Silberberg, *Opt. Express* **13**, 1468 (2005).
13. H. Dana and S. Shoham, *Opt. Express* **19**, 4937 (2011).
14. M. E. Durst, G. H. Zhu, and C. Xu, *Opt. Express* **14**, 12243 (2006).
15. K. Lou, S. Granick, and F. Amblard, *Proc. Natl. Acad. Sci. USA* **115**, 6554 (2018).
16. C. Xu and W. W. Webb, *J. Opt. Soc. Am. B* **13**, 481 (1996).
17. H. J. Choi and P. T. C. So, *Sci. Rep.* **4**, 6626 (2014).
18. C. Y. Chang, Y. Y. Hu, C. Y. Lin, C. H. Lin, H. Y. Chang, S. F. Tsai, T. W. Lin, and S. J. Chen, *Biomed. Opt. Express* **7**, 1727 (2016).
19. C. G. Durfee, M. Greco, E. Block, D. Vitek, and J. A. Squier, *Opt. Express* **20**, 14244 (2012).
20. P. Theer and W. Denk, *J. Opt. Soc. Am. A* **23**, 3139 (2006).
21. H. Dana, A. Marom, S. Paluch, R. Dvorkin, I. Brosh, and S. Shoham, *Nat. Commun.* **5**, 3997 (2014).
22. E. Tal, D. Oron, and Y. Silberberg, *Opt. Lett.* **30**, 1686 (2005).
23. A. M. Weiner, *Ultrafast Optics* (Wiley, 2009).
24. X. L. Wang, J. P. Ding, W. J. Ni, C. S. Guo, and H. T. Wang, *Opt. Lett.* **32**, 3549 (2007).
25. C. Akcay, P. Parrein, and J. P. Rolland, *Appl. Opt.* **41**, 5256 (2002).